

The Magnetic Properties of Heating Events on High-Temperature Active Region Loops

IGNACIO UGARTE-URRA,¹ NICHOLAS A. CRUMP,¹ HARRY P. WARREN,¹ AND THOMAS WIEGELMANN²

¹*Space Science Division, Naval Research Laboratory, Washington, DC 20375*

²*Max-Planck-Institut für Sonnensystemforschung, Justus-von-Liebig-Weg 3, 37077 Göttingen, Germany*

ABSTRACT

Understanding the relationship between the magnetic field and coronal heating is one of the central problems of solar physics. However, studies of the magnetic properties of impulsively heated loops have been rare. We present results from a study of 34 evolving coronal loops observed in the Fe XVIII line component of AIA/SDO 94 Å filter images from three active regions with different magnetic conditions. We show that the peak intensity per unit cross-section of the loops depends on their individual magnetic and geometric properties. The intensity scales proportionally to the average field strength along the loop (B_{avg}) and inversely with the loop length (L) for a combined dependence of $(B_{avg}/L)^{0.52 \pm 0.13}$. These loop properties are inferred from magnetic extrapolations of the photospheric HMI/SDO line-of-sight and vector magnetic field in three approximations: potential and two Non Linear Force-Free (NLFF) methods. Through hydrodynamic modeling (EBTEL model) we show that this behavior is compatible with impulsively heated loops with a volumetric heating rate that scales as $\epsilon_H \sim B_{avg}^{0.3 \pm 0.2} / L^{0.2 \pm 0.1}$.

Keywords: Sun: corona

1. INTRODUCTION

Understanding the relationship between the magnetic field and coronal heating is one of the central problems of solar physics. It is well established that in the regions on the Sun where the surface magnetic fields are stronger, the plasma in the atmosphere reaches higher temperatures and emits larger amounts of ultraviolet and X-ray radiation. Global quantities such as the luminosity or the total radiance scale up with the total unsigned magnetic flux of the regions through power-law relationships (e.g. Schrijver 1987; Fisher et al. 1998; Benevolenskaya et al. 2002; Fludra et al. 2002; Pevtsov et al. 2003; Fludra & Ireland 2008).

The atmosphere, frozen-in to the magnetic field, responds to the long term changes that the surface flows impose on the magnetic elements. Over time, major reorganization of the fields result in follow-up changes in the morphology of the coronal emission and the radiance (e.g. van Driel-Gesztelyi & Green 2015; van Driel-Gesztelyi et al. 2003; Démoulin 2004; Ugarte-Urra et al. 2015).

At the time scale of minutes, the magnetic field distributions evolve slowly. Subject to flows of $\sim 1 \text{ km s}^{-1}$ (e.g. Berger & Title 1996), a $5''$ flux element experiences a modest displacement of about its own size within an hour. In that interval, coronal emission in an active region can evolve rather quickly with as many as five heating events as observed in spectral lines formed around the 3–5 MK temperature (Ugarte-Urra & Warren 2014). The atmospheric re-

sponse at the chromospheric footpoints of the loops is even more rapid (Testa et al. 2014). The challenge for coronal heating is, therefore, understanding the coupling between the forcing that convection motions impose to the magnetic field and the response of the atmosphere.

As surface flows carry the energy, their presence provides clues about where this energy can be deposited. For example, in the umbra of sunspots flows are inhibited (e.g. Borrero & Ichimoto 2011), therefore it is not surprising to see most coronal loops rooted outside them. Tiwari et al. (2017) have shown that the occasional loops observed with one footpoint rooted in umbra have the opposite footpoint anchored in plage or penumbra. Field line tangling followed by reconnection (see review Klimchuk 2015), and wave dissipation (see review Arregui 2015) have been the traditional heating scenarios considered for the transfer of energy. The observational constraints, however, are yet insufficient to rule out any of these models.

In this study, we investigate the coupling between magnetic fields and radiance. Our goal is to provide insight on how the magnitude of the heating scales up with the properties of the local magnetic field once the heating mechanism is already in place. There are two key properties of the field that are important to this coupling: magnetic field strength (B) and loop geometry (L). This is discussed in detail in Mandrini et al. (2000), where following the theoretical implications of SXT/Yohkoh loop diagnostics discussed by Porter & Klimchuk (1995), they compile a list of poten-

tial heating mechanisms and how each depends on quantities such as magnetic field strength, loop length, velocity and density. While, in principle, this implies that observational constraints on the scaling can help us discriminate between models, the effectiveness of this method as a final discriminator is still not guaranteed (see discussion in [Mandrini et al. 2000](#); [Klimchuk 2006](#)).

The studies that have looked into these constraints, nevertheless, have demonstrated that such a parameterization of heating can be very successful in reproducing several aspects of coronal emission. Forward modeling of active regions and the full Sun as an ensemble of hydrodynamic loops using a volumetric heating rate that scales as a function of the average magnetic field strength in the loop and its length ($\epsilon_H \propto B_{avg}^\alpha/L^\beta$) has been successful in reproducing relationships for global quantities. Several of these studies find $\alpha = 1$ and $\beta = 1$ to be a good prescription to reproduce the emission of hot ($\gtrsim 3$ MK) loops at the core ([Warren & Winebarger 2006, 2007](#); [Lundquist et al. 2008](#); [Ugarte-Urra et al. 2017](#)), but they have problems replicating the emission of cooler 1-2 MK emission. [Winebarger et al. \(2008\)](#) showed that attempting to match the cool moss emission can lead to a different scaling ($B_{avg}^{0.3}/L$). Furthermore, modeling the full Sun, [Schrijver et al. \(2004\)](#) found a power-law dependence (B_0/L^2) on footpoint field strength B_0 (see also [Dudík et al. 2011](#)), which [Warren & Winebarger \(2006\)](#) argued to be consistent as they obtained $B_{avg} \sim B_0/L$.

In our study, we revisit this problem by taking advantage on the progress made in recent years in our ability to first observe loops at high spatial resolution, high temporal resolution and temperature discrimination, and then model their magnetic topology with improved magnetic models of the atmosphere. The objectives are two-fold: obtain novel constraints on how observational properties like the radiance at high temperatures for specific stages in the evolution of an individual loop scale with B and L ; and relate those results to the demands imposed on the volumetric heating rate.

In Section 2 we describe the dataset and methods used to extract the magnetic and radiative properties of 34 coronal loops from three active regions. Section 3 presents the results of comparing the two properties for all loops. The implications of those results for coronal heating are discussed in Section 4. We find that, at the scale of individual loops, the intensities from the Fe XVIII 93.93 Å indeed depend on the individual properties of the loops and scale proportionally with the average field strength of the loop and inversely with its length. We provide new constraints for models of heating in the corona.

2. METHODS

This paper is a follow up to [Warren et al. \(2018\)](#), from now on [Paper I](#), an investigation that compared loops traces in

coronal images with field lines computed from various magnetic field extrapolation methods. [Paper I](#) used a list of 15 active regions, first compiled in a study of high temperature emission in active region cores ([Warren et al. 2012](#)). The current investigation extends the analysis of the magnetic topology to find a link to the plasma properties of selected loops in a subset of the active regions. Where not explicitly stated, the observations and methods are the same as those described in [Paper I](#).

2.1. Dataset

Our dataset consists of 34 loops from a subset of three active regions (NOAA 11158, 11190, 11339) from the active region list in [Paper I](#). The full list includes regions that span one order of magnitude in total unsigned magnetic flux. These three active regions were selected because they cover most of the magnetic flux range (4.2×10^{21} Mx, 1.8×10^{22} Mx, 2.6×10^{22} Mx, respectively); and a visual inspection of the coronal images shows well defined loop structures that are suitable for the identification, manipulation and quantitative analysis described in Section 2.

For each active region we downloaded cutouts from the *Solar Dynamics Observatory* ([Pesnell et al. 2012](#)) Joint Science Operations Center¹ for a one-hour interval. The downloads included data from the Atmospheric Imaging Assembly (AIA, [Lemen et al. 2012](#)) at 12 s cadence in several EUV channels, plus line-of-sight and vector magnetograms from the Helioseismic and Magnetic Imager (HMI, [Scherrer et al. 2012](#)) at 45 s and 720 s cadence, respectively.

Unlike [Paper I](#) that looks at the loops in several of the AIA bandpasses, in this study, we only considered what we call AIA Fe XVIII images. These are images from the 94 Å channel that have been processed to isolate and retain the emission from the Fe XVIII 93.93 Å spectral line, while removing the contribution from cooler lines (see all contributions in [O'Dwyer et al. 2010](#)). The empirical correction (equation 1 in [Ugarte-Urra & Warren 2014](#)) was devised by [Warren et al. \(2012\)](#). We chose Fe XVIII because we consider it an optimal choice for plasma diagnostics in active region loops with current instrumentation. Fe XVIII images can be obtained frequently and at high resolution with AIA. The spectral line forms within the temperature range 3 - 7 MK where active region cores peak in their emission measure ([Warren et al. 2012](#)). Furthermore, we have shown that the intensity peak in this line takes place before the loop reaches the equilibrium point, when radiation starts to dominate the cooling in an impulsively heated loop ([Ugarte-Urra et al. 2017](#)). Observing before the start of the radiative cooling phase is important in our ability to diagnose the heating properties ([Winebarger & Warren 2004](#)).

¹ <http://jsoc.stanford.edu/>

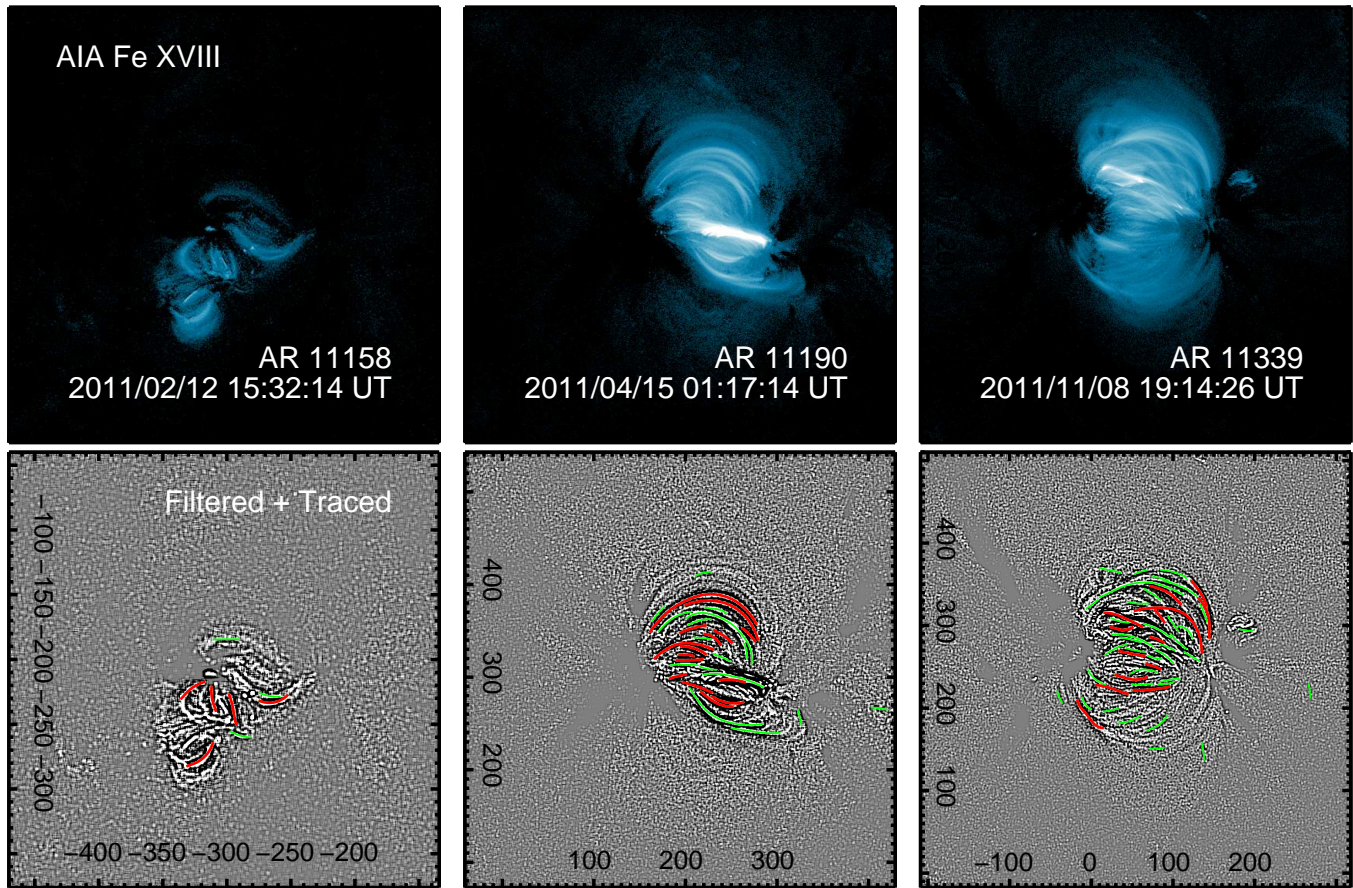


Figure 1. Coronal loops identified using the automated loop tracing algorithm for all three active regions. The top row shows the AIA Fe XVIII eight-image average that served as input. All regions are shown at the same logarithmic intensity scaling. The bottom row shows the resulting filtered image with the automatically identified traced segments on top. The red lines represent the subset of the segments selected for the full topological and radiative analysis. Solar coordinates are provided in arcseconds from disk center.

2.2. Loop identification

Loops in the AIA Fe XVIII images were identified using the Oriented Coronal CURved Loop Tracing (OCCULT-2) algorithm (Aschwanden 2010; Aschwanden et al. 2013). The algorithm uses a low-pass filter to eliminate noise and a high-pass filter to enhance the fine structure. Combined through subtraction they operate as an unsharp masking filter that reveals ridges that can be traced. Starting from the highest contrast locations, loops are identified, and then erased from the images to allow the procedure to be repeated, and loops accumulated until reaching the threshold level for detection.

Following Paper I, and to improve signal-to-noise, we applied this method to an eight-image average (96 s interval) at the middle time of the observing sequence for all three active regions. Our choice of time is different than Paper I, where the start time was selected. This change is motivated by our need to investigate the loop evolution before and after the time of identification. We identified 8, 31, and 51 loops in NOAA 11158, 11190 and 11339 respectively. Note that the number of identifications correlates with the total Fe XVIII

emission in the regions (Warren et al. 2012). The traced loop segments are shown in Figure 1. This number is larger than the number of loops used in our full analysis because we introduce further constraints in the selection based on the analysis of the topology and the intensity evolution. We provide further details in sections 2.3 – 2.5.

2.3. Magnetic field extrapolations

The magnetic properties of the loops were determined from magnetic models of the active regions. We considered three magnetic field extrapolation techniques: a simple potential field extrapolation, the Non Linear Force-Free (NLFF) field extrapolation method of Wiegmann et al. (2012), and the Vertical-Current Approximation VCA-NLFF method described in Aschwanden (2016). The three methods are described in some detail in Paper I, here we summarize the basic assumptions.

The potential approximation assumes a current-free volume and solves the field equations ($\nabla \times \mathbf{B} = 0$, $\nabla \cdot \mathbf{B} = 0$) using the corrected line-of-sight component of the observed magnetic field as a lower boundary. Solutions are obtained by

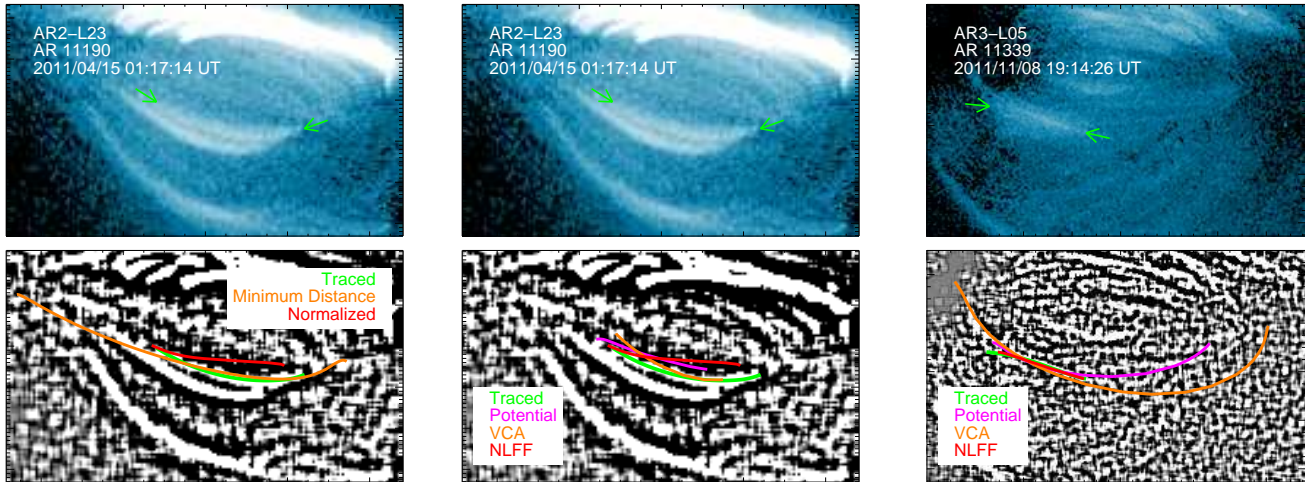


Figure 2. The left panel shows a loop where the best field line match for a traced loop is better achieved by using a metric where distances along the loop and field line are first normalized by distance to one footpoint. The middle panel shows differences in the best field line match for that same loop and three extrapolation methods (potential, VCA and NLFF). These differences can sometimes be significant, as the right panel shows for a different loop in a different active region. In those cases inspecting the temporal evolution of the loop helps understanding what model works best for that traced loop. The green arrows indicate the location of the traced loop.

means of Fourier transforms as in our previous studies of the topology of active regions in connection to coronal heating (Warren & Winebarger 2006; Ugarte-Urra et al. 2017) and the initiation of coronal mass ejections (Ugarte-Urra et al. 2007). We use HMI line-of-sight magnetograms as the boundary layer.

Force-free magnetic models do allow currents in the volume, but neglect all non-magnetic forces (e.g. Wiegelmann & Sakurai 2012). The field equations are solved assuming a vanishing Lorentz force $\mathbf{J} \times \mathbf{B} = 0$, that leaves us with $\nabla \times \mathbf{B} = \frac{4\pi}{c} \mathbf{J} = \alpha \mathbf{B}$, and $\nabla \cdot \mathbf{B} = 0$. This approximation is called Non-Linear Force-Free (NLFF), and the twist parameter α changes throughout the volume as $\mathbf{B} \cdot \nabla \alpha = 0$. We obtain solutions using the code developed by Wiegelmann et al. (2012). As a constraint we use HMI photospheric vector magnetic fields that are preprocessed to create a boundary condition that is consistent with the force-free field assumption.

The VCA-NLFF code uses the line-of-sight magnetogram as the boundary and assumes that the magnetic field can be decomposed into a superposition of magnetic charges below the surface with a non-potential field prescribed by a helical twist. The code optimizes the non-potential parameters of the model by comparing the field lines to the traced loops obtained from a call to the OCCULT-2 loop identification algorithm. As in Paper I, and only for this module, we use data from all the following AIA channels: 94, 131, 171, 193, 211, 335 Å.

For each active region we use the extrapolations calculated for Paper I at the start of the one hour observing sequence. The output of the three methods is the magnetic field decomposed in Cartesian coordinates. Field lines were calculated

for seeds from all magnetogram pixels with a magnetic flux density above 25 G. The field line integrator uses a fourth-order Runge-Kutta method with adaptive step size, written in C.

2.4. Mapping field lines to traced loops

To determine the field line that best matches any given traced loop we used two metrics. The default metric in our work flow is the “mean minimum distance” defined in Paper I. This distance is the average minimum Euclidean distance between reference points along the full length of the traced loop and the field line. This metric works well in most loops, determined by visual inspection. In 7 of the 34 cases we resorted to a second metric that normalizes the distance along the traced loop and the field line before evaluating the distance between the points. We developed this approach for a previous study (Ugarte-Urra et al. 2006) where we found that, when there are good constraints on the footpoints, it can help get around misidentifications due to some degeneracy introduced by projecting 3D field lines to an image plane. By comparing proportional distances from the end points, it helps in discarding longer loops that may project a section of their length onto the traced loop, resulting in a small Euclidean metric, but an overall incorrect match for the loop.

We determined the best fits for all identified loops with the two metrics, but only adopted the “normalized distance” metric solution when there were obvious visual cues that this method provided a better match. The left panel in Figure 2 shows one example for a NLFF extrapolation. In this case the minimum distance method returns a field line that despite running along most of the traced loop axis, clearly extends many pixels beyond its observed footpoints. The second met-

Table 1. Loops dataset. The magnetic properties listed here are derived from the selected best-fit field line of the three extrapolation models. The Fe XVIII properties are derived from the observed loops identified in the AIA images. The loops have a code identifier that links them to one of the three active regions in the sample, and the list of loop segments identified for that region. The magnetic properties for the best-fit solution of all methods are underlined. The properties are in bold font for the field line selected from visual inspection of the best-fits.

NOAA	Time [UT]	Loop		Magnetic Properties						Fe XVIII Properties			
				B_{avg} [G]			Length ["]			Time [UT]	Intensity		Width [pixels]
		#	Code	PFE	VCA	NLFF	PFE	VCA	NLFF		[^a]	[^b]	
11158	2011/02/12 15:01:57	1	AR1-L00	89	114	<u>138</u>	74	51	<u>69</u>	15:26:14	60	16.0	2.66
		2	AR1-L01	<u>195</u>	116	286	<u>64</u>	92	35	15:32:26	9	12.3	0.93
		3	AR1-L02	134	<u>110</u>	111	26	<u>32</u>	28	15:19:50	25	20.6	1.42
		4	AR1-L03	78	92	<u>86</u>	29	22	<u>23</u>	15:32:14	8	10.6	1.36
		5	AR1-L04	101	<u>60</u>	78	81	<u>199</u>	211	15:31:02	26	8.7	2.44
11190	2011/04/15 00:47:05	6	AR2-L01	324	380	860	66	55	52	01:15:02	259	223.2	1.40
		7	AR2-L02	205	208	310	128	115	121	01:17:50	12	19.0	1.02
		8	AR2-L03	264	256	<u>244</u>	48	30	<u>95</u>	01:11:38	16	15.0	1.34
		9	AR2-L05	198	143	173	147	185	199	01:19:26	17	18.7	1.34
		10	AR2-L06	74	66	<u>132</u>	144	428	<u>164</u>	01:18:14	10	5.9	1.67
		11	AR2-L07	133	147	<u>90</u>	83	91	<u>325</u>	01:22:38	11	8.2	1.62
		12	AR2-L11	113	97	160	130	137	162	01:13:38	37	18.8	1.87
		13	AR2-L13	194	172	203	51	54	99	01:17:26	6	12.8	1.12
		14	AR2-L14	120	109	<u>137</u>	116	111	<u>113</u>	01:18:26	14	15.2	1.23
		15	AR2-L16	345	309	<u>581</u>	20	15	<u>110</u>	01:18:38	7	21.8	0.79
		16	AR2-L17	128	162	<u>195</u>	61	76	<u>101</u>	01:17:26	6	9.3	1.07
		17	AR2-L23	352	347	476	33	33	41	01:16:38	34	31.3	1.47
		18	AR2-L26	298	226	59	38	70	384	01:10:14	251	175.6	1.55
19	AR2-L28	259	253	330	31	25	53	01:14:50	59	56.0	1.32		
20	AR2-L29	329	287	<u>458</u>	31	22	<u>28</u>	01:17:50	19	42.5	0.87		
11339	2011/11/08 18:44:43	21	AR3-L00	209	177	201	61	47	54	19:14:50	74	37.1	1.86
		22	AR3-L01	203	294	208	86	109	37	19:16:02	85	58.0	1.57
		23	AR3-L02	311	416	<u>523</u>	113	64	<u>90</u>	19:14:26	20	21.0	1.30
		24	AR3-L05	286	198	235	120	229	42	19:14:02	18	15.7	1.39
		25	AR3-L07	154	116	143	289	355	320	19:13:02	11	7.8	1.43
		26	AR3-L08	<u>382</u>	275	338	<u>38</u>	45	40	19:12:02	15	20.4	1.10
		27	AR3-L11	138	86	<u>158</u>	181	462	<u>290</u>	19:14:14	8	5.7	1.46
		28	AR3-L15	423	433	<u>491</u>	72	48	<u>76</u>	19:08:50	12	12.9	1.25
		29	AR3-L16	173	181	189	67	86	184	19:14:50	5	9.9	0.92
		30	AR3-L19	142	107	152	284	342	258	19:14:26	16	4.7	2.27
		31	AR3-L23	<u>348</u>	409	364	<u>36</u>	66	35	19:14:26	52	19.9	2.09
		32	AR3-L24	172	127	<u>219</u>	122	277	<u>118</u>	19:14:02	19	6.4	2.24
		33	AR3-L27	277	309	275	139	92	172	19:12:26	4	4.4	1.29
		34	AR3-L32	99	84	<u>163</u>	177	515	<u>254</u>	19:14:50	23	4.5	3.13

^aDN s⁻¹pixel⁻¹

^bDN s⁻¹pixel⁻¹Mm⁻²

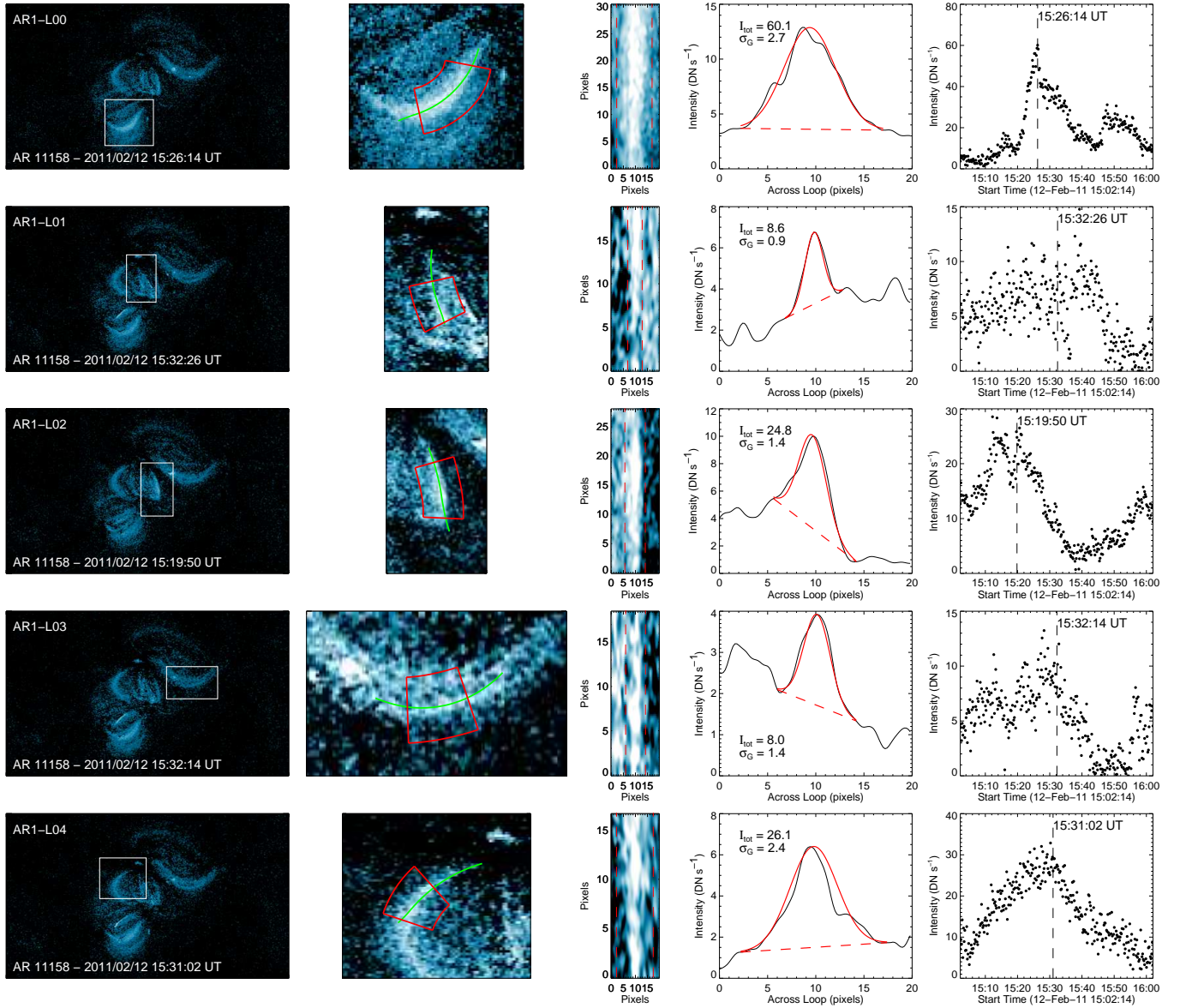


Figure 3. Summary of the analysis performed on the loop segments in active region 11158. Labels in the images can be used to link to the loop properties in Table 1. The left panels show a wide angle and close-up look at the AIA Fe XVIII images of each loop. Cross-sectional loop intensities along the loop axis are extracted to form a straightened image in a reduced field-of-view (red box). The averaged profile is then fitted with a Gaussian (solid red line) over a linear background (red dashed line). Finally, the integrated intensity is plotted as a function of time. The local intensity peak closest in time to the time of identification (middle of the sequence) is saved for comparison to the magnetic properties. The solid green line outlines the location of automatic loop segment identification used in the magnetic topology analysis.

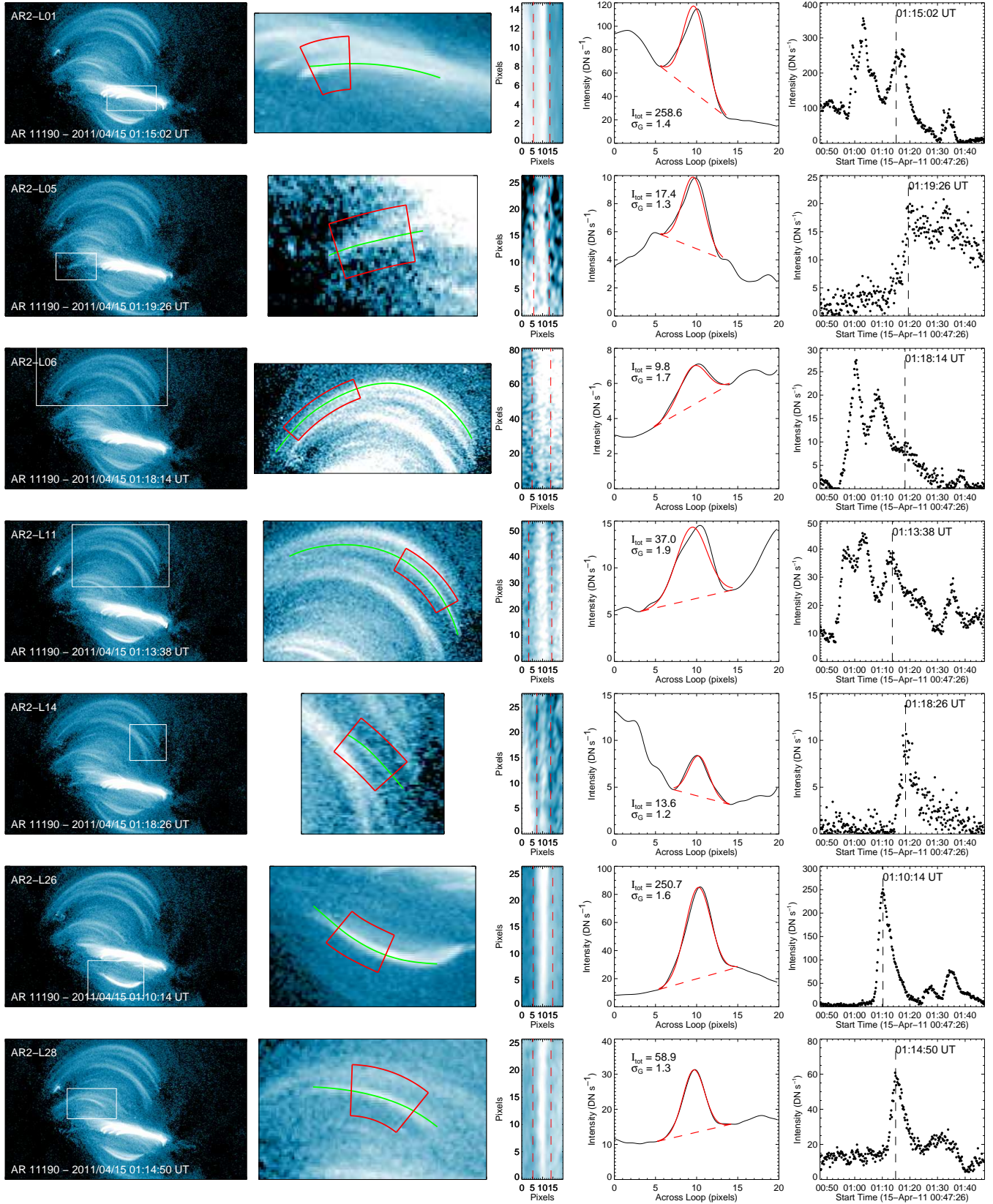


Figure 4. Same as Figure 3 for active region 11190. We show here seven of the fifteen loops studied in this region.

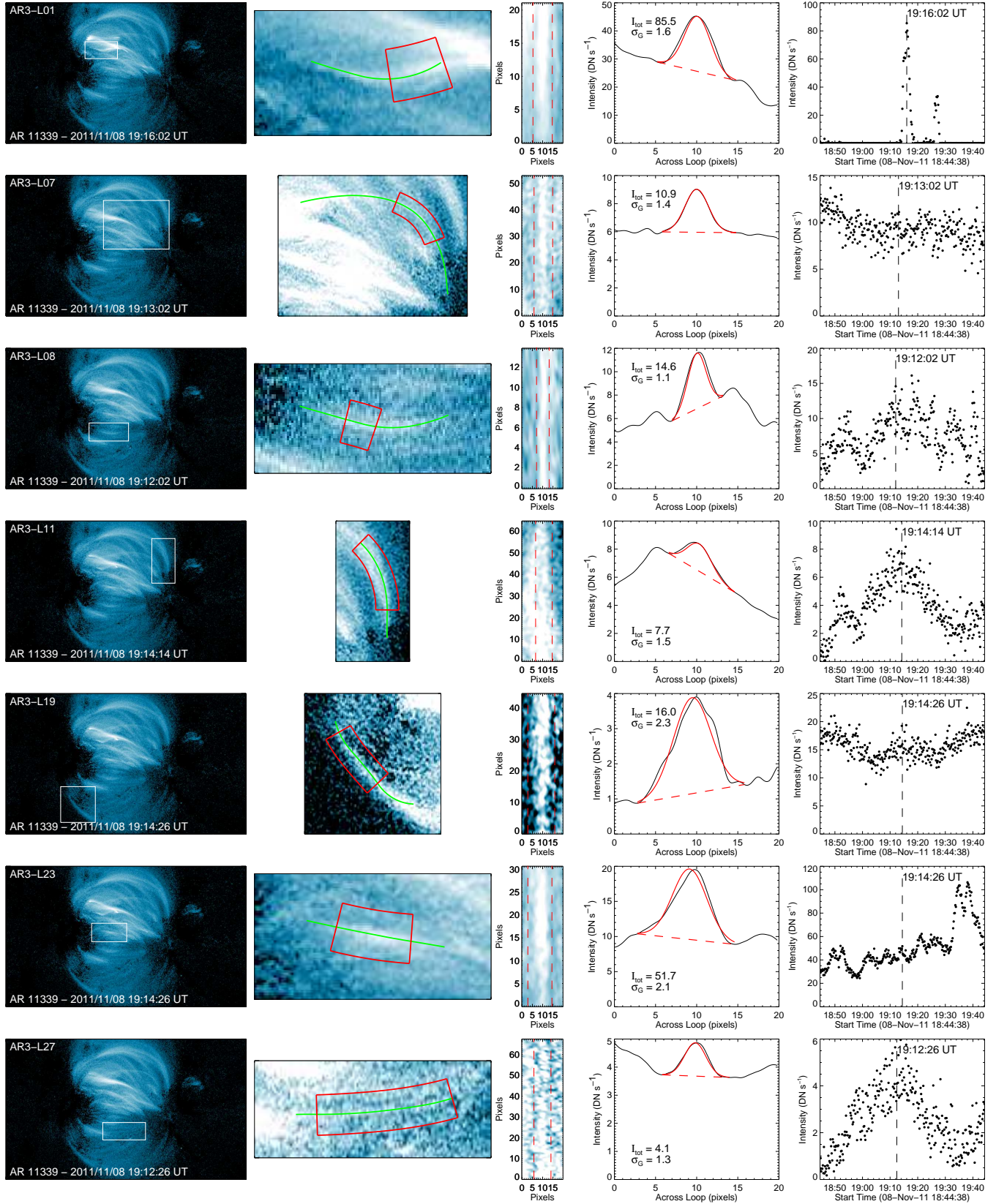


Figure 5. Same as Figure 3 for active region 11339. We show here seven of the fourteen loops studied in this region.

ric for this loop returns a smaller field line that, while it does not provide as good a fit along the axis, we argue that it provides a better representation of the overall topology (footpoints and projected length) and therefore a preferred choice to estimate the loop's field strength and length. Loops that had no satisfactory best-fit field line from either of the metrics were discarded. This is one of the reasons why the number of loops in the analysis is smaller than the number of loop segments automatically identified. There were also cases where multiple loop segments corresponded to the same loop, and we retained the longer ones.

Paper I provides a systematic comparison between the extrapolation methods, their ability to reproduce the topology of observed coronal loops, and discusses the best overall performance. At the individual loop level we find that no single method provides the best match for all loops. Table 1 lists the complete set of loops in this analysis including the average field strength (B_{avg}) and loop length from all three extrapolation methods. The loops are numbered and have a code identifier that links them to the active region and the list of loop segments identified for that region. The magnetic properties for the extrapolation with the smallest minimum distance metric are underlined. The majority are under the NLFF approach, consistent with Paper I. Figure 2 shows examples of the different outcomes for the field line identification from the three methods. We encounter numerous examples where the solutions are very consistent between the three methods, such as loop #17 (AR2-L23) in Figure 2, but there are also examples where the discrepancies are significant, e.g. loop #24 (AR3-L05) also in the figure. In a few cases, such as loop #28 (AR3-L15) shown in Figure 2, a visual inspection (space and time) reveals that the loop is best represented by the best-match field line of an extrapolation (VCA) with a metric value that it is not the smallest (NLFF). For that reason, we also highlight in Table 1 with bold font the field line selected based on visual inspection of the best-fits for the three methods. Bold (visual) and underlined (purely metric) selections coincide in fifteen cases and in several others the differences between the properties are minor. This will become apparent later on when we present the results as a scatter plot. The inconsistencies ultimately expose the difficulties we faced in disentangling the projections of a 3D volume of field lines onto the plane of the image. This is particularly important when loops do not have well identified footpoints and segments cannot impose those constraints on the field line fitting.

2.5. EUV Intensities

The objective of our study is to investigate the coupling between the loop's magnetic properties and their radiative output. To characterize the latter, we use the AIA Fe XVIII images. The simplest approach would be to record the intensi-

ties of the loops at the time of identification. However, given our hydrodynamic and observational understanding of coronal loop evolution, this diagnostic seems insufficiently constrained. Loops are often evolving, changing their brightness, even appearing and disappearing from a particular bandpass (e.g. Winebarger & Warren 2005; Ugarte-Urra et al. 2009; Viall & Klimchuk 2012). This behavior is understood as the signature of changing dynamics in their plasma properties with significant variations in density and temperature (e.g. Reale 2014). A single snapshot is then likely to portray many loops at different stages of their evolution. As we intend to compare the intensities for all the loops, we decided to record the count rates at one particular predetermined instant in their evolution, the same for all, at the peak in their lightcurves.

The loop intensities are calculated in several steps. We employ an interactive graphical user interface (GUI) developed by us in IDL. Earlier versions of the tool have been used extensively to obtain loop widths and intensities in AIA, EIS/Hinode and Hi-C data (Warren et al. 2008; Brooks et al. 2012, 2013). Figures 3–5 show examples of the figures and products generated by the program. The GUI first imports the location of the automatically detected loop segments to identify the loops in the AIA images. This is shown by a green line in the second panel of the figures. This is only done for the loops that already survived the topological analysis. For every image in the AIA sequence, the back-end of the program extracts the intensity profiles across the loop axis, defined here by the imported locations, and along the full length of the segment, creating an interpolated straightened image of the loop as shown in the third panel of the figures. The length of this new loop segment is sometimes smaller than the original outline. This resizing of the areas of interest (red box in the figures) was necessary to avoid as much as possible contamination from neighboring loops along the full temporal sequence. The GUI shows the evolution in time of the AIA images with respect to those choices and allows for interactive changes. Intensity profiles are averaged along the loop axis and two background points are manually selected as part of a Gaussian fit to the loop cross-section. Finally, the integrated Gaussian intensity for every image is computed and plotted as a function of time (right-most panel in the figures).

We performed this analysis for all loop segments. Several loops had to be discarded because they were too weak to provide an averaged loop cross-section that could be fitted. Figures 3–5 show representative cases for all three regions. Table 1 shows the resulting intensities and widths for all the loops. The intensities correspond to the local peak closest in time to the middle of the sequence, the time where the automatic loop identification algorithm was applied. As the emission in coronal plasmas depends on the volume of the emitting structure, to compare the intrinsic emission from loops

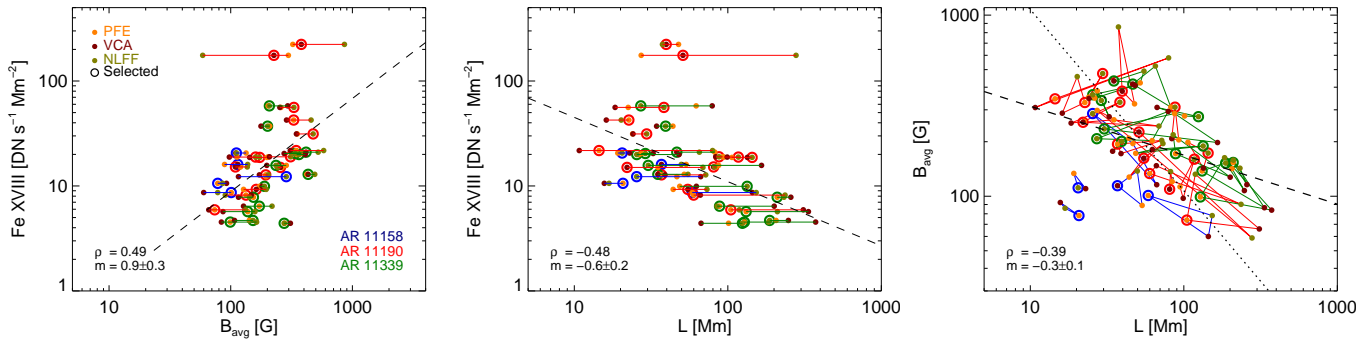


Figure 6. Relationship between Fe XVIII intensity, average field strength (B_{avg}) and loop length (L) for all 34 loops in the sample presented in Table 1. Filled circles in different colors indicate the extrapolation method used in computing the values. Solutions for a single loop are joined by a solid line. Open circles highlight the solution, out of the three, selected from visual inspection of the best fitted field lines. Colors of open circles and solid lines indicate the active region to which the loop belongs to. Correlation coefficient (ρ) and slope (m) of the power-law fit to the open circles are provided on the legend. The dotted line on the right panel corresponds to a slope of $m = -1$ and it is provided for context.

with different integration paths we divide the count rates by the cross-sectional area. We assume circular cross-sections with a diameter that is twice the Gaussian standard deviation. This is presented in Table 1 in units of DN s⁻¹ Mm⁻².

Most loops exhibit lightcurves characteristic of transient events: a rising phase, followed by a peak and a decaying phase within the short observing window. There are, however, a few cases such as AR3-L07 (Figure 5), where the lightcurve remains mostly constant. Long-lived loops have been observed before (e.g López Fuentes et al. 2007; Scott et al. 2012), particularly at high temperatures. In our dataset, transients are more common.

Our ability to subtract the background intensity is one of the main sources of uncertainty in measuring the intensities of the loops. The spread of the data points in time in the lightcurves gives us an estimate of the uncertainties in the measurement, which goes from 50% in a weak loop (AR3-L27) to 2% in a bright one (AR2-L26).

3. RESULTS

In this section we describe how the various properties of the loops (radiative, magnetic, geometrical), obtained through the methods presented earlier, scale with each other.

The left panel in Figure 6 shows how the peak in Fe XVIII intensity scales with the average magnetic field strength (B_{avg}) for all loops in the three active regions. In the figure, each loop has three B_{avg} values, joined by a solid line, corresponding to three extrapolation methods presented in Table 1. This provides an impression on the level of precision we achieve in determining this quantity using three standard models to describe the magnetic properties of loops in the corona. There are no systematic differences between the three, which suggests that the results of this study are largely independent of the magnetic model. Note, however, that we have not tested the accuracy of the models. The large open circles highlight our preferred solution from visual inspection

of the three best-matched field lines, i.e. the values in bold font in Table 1. We use only these points in any subsequent calculations. We find that there is a correlation of $\rho = 0.49$ between the Fe XVIII intensity and B_{avg} . A linear fit to the selected points returns a power-law relationship with a slope of $m = 0.9 \pm 0.3$. As we average the counts from many pixels along and across every loop, systematic error dominate over the statistical uncertainties in the intensities. The fit parameters are reproducible when we fit a subset of the data points with a Monte Carlo approach. We obtained the same slope and standard deviation from the histogram of solutions to fits of 100 random combinations of 25 data points.

The middle panel shows how the Fe XVIII intensity scales with loop length. They are anticorrelated ($\rho = -0.48$) which confirms the general visual impression from coronal images that the longer the loops are, the fainter they emit at these wavelengths.

Two data points at large intensities (AR2-L01, AR2-L26) appear outliers to the general trend in both panels. We can not explain their excess of counts (factor of 4) by uncertainties in the fits to the loop intensities. The signal is high and the profiles are clean. One possibility is that we have underestimated the volume of emission by assuming a circular cross-section. Multiple loops brightened up at the same time nearby, and while we removed the background, an alignment along the line-of-sight can not be ruled out. The other possibility is that the change in behavior is real and needs a physical explanation. As we do not have a reason to discard them, we keep the two points as part of the analysis.

The right panel in Figure 6 shows the relationship between field strength and loop length. This relatively complex figure shows the same information as previous panels, but now the three topological solutions for a particular loop constitute the three vertices of a triangle joined by a solid line. The closer the vertices, the better agreement between the methods. The spread of the solutions shows that, despite the

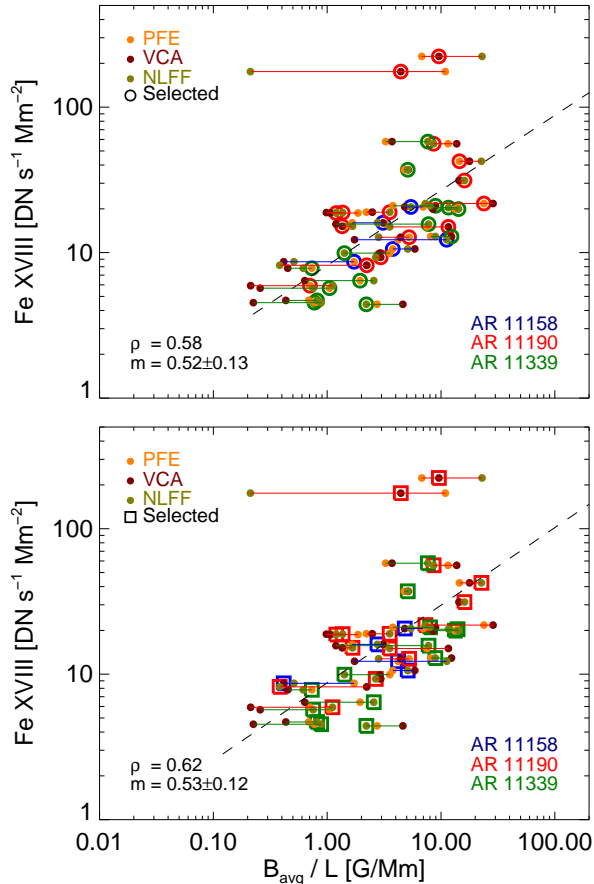


Figure 7. Relationship between Fe XVIII intensity and the B_{avg}/L ratio for all 34 loops in the sample. Symbols and colors are the same as in Figure 6. The top panel highlights with open circles the solution selected, out of the three extrapolation methods, from visual inspection of the best fitted field lines (bold font values in Table 1). The bottom panel highlights with open squares the solution with the smallest metric (underlined values in Table 1).

general agreement in the dependencies of the intensity with B_{avg} and L , there can be significant differences between the $[B_{avg}, L]$ pairs for each method. The correlation coefficient is $\rho = -0.39$ for the overall set of points with a slope of $m = 0.3 \pm 0.1$. For reference, Mandrini et al. (2000) found slopes of -0.97 ± 0.25 using all field lines in their extrapolations within predetermined thresholds, but not isolating the ones linked to emitting loops. The dotted line shows a slope of -1 for context. The loops in our sample are not a distinct population within the general distribution of B_{avg} and L , except for having average field strengths that are consistently larger than ~ 100 G.

In Figure 7 we show the dependence of Fe XVIII intensity as a function of the B_{avg}/L ratio. The top panel shows the fits for the selection of best visual solutions as in Figure 6. The correlation clearly increases with the combined dependence ($\rho = 0.58$). As in the previous panels the linear fit

Table 2. Correlation coefficient and slope of the power-law fit to the Fe XVIII intensity dependence on the following quantities

	ρ	m
L	-0.48	-0.6 ± 0.2
B_{avg}	0.49	0.9 ± 0.3
B_{apex}	0.55	0.7 ± 0.2
B_f	0.02	0.0 ± 0.3
B_{fmax}	0.02	0.0 ± 0.3
B_{fmin}	0.18	0.3 ± 0.3
B_{avg}/L	0.58	0.5 ± 0.1
B_{apex}/L	0.57	0.4 ± 0.1
B_f/L	0.50	0.6 ± 0.2
B_{fmax}/L	0.47	0.6 ± 0.2
B_{fmin}/L	0.52	0.5 ± 0.2

($m = 0.52 \pm 0.13$) is not satisfactory for all data points, but we prefer to leave any non-linear description to future samples with more points on the the high intensity end. In the bottom panel, we show the same exact figure but highlighting with open squares the solutions with the absolute smallest distance metric. The results overlap and demonstrate that the trends are robust and not subject to any bias introduced in the visual selection.

In Table 2 we show the correlation coefficients and slopes for these quantities and others that we also considered. We include the magnetic field strength at the apex of the loop (B_{apex}) and at the footpoints: as an average (B_f), the maximum (B_{fmax}), and the minimum (B_{fmin}). We find the field strength at the footpoints to be uncorrelated to the Fe XVIII intensity of the loops. The results for the apex are interesting because they exhibit the highest correlation for any field strength measurement. This may, however, be driven by the anticorrelation between B_{apex} and loop length ($\rho = -0.63$). In fact, B_{apex}/L is not a better proxy for Fe XVIII intensity than B_{avg}/L .

4. DISCUSSION

There have been many studies that have shown that the luminosity or the total radiance of active regions and other features on the Sun scale up with the total unsigned magnetic flux as a power-law relationship (e.g. Schrijver 1987; Fisher et al. 1998; Benevolenskaya et al. 2002; Fludra et al. 2002; Pevtsov et al. 2003; Fludra & Ireland 2008). Models of these regions as the sum of individual loops with a prescribed volumetric heating rate of the form $\epsilon_H \propto B^\alpha/L^\beta$, where α and β are positive, have been successful at describing global intensities. The actual values of those

exponents have been a source of debate in the literature: Schrijver et al. (2004); Warren & Winebarger (2006, 2007); Lundquist et al. (2008); Winebarger et al. (2008); Dudík et al. (2011); Ugarte-Urra et al. (2017). Recent 3D MHD resistive simulations of magnetic flux tubes shuffled at their footpoints also predict that loop properties such as the temperature should scale proportionally with magnetic field strength and to a lesser degree with the inverse of the loop length (Dahlburg et al. 2018).

In that context, the main result of our study, the scaling of the loop’s radiance with magnetic field strength and the inverse of the loop’s length is not unexpected. It is, nonetheless, an independent estimate that had not been established yet. The novelty stands in that we use measurements of individual loops (intensities, cross-sections), that are then combined with the still unavoidable magnetic models that previous studies already used. We link for the first time at these wavelengths the peak emission of what we interpret as a heating event in an evolving loop structure to its magnetic properties. A similar loop survey was recently carried out by Xie et al. (2017), who looked at the spectroscopic and magnetic properties of 50 active region loops with temperatures ≤ 2 MK. While the spectral analysis allowed them to obtain valuable plasma properties such as velocity and density, that study lacks the temporal resolution to investigate the evolution in time that we argue here is critical for our purposes of characterizing the same evolutionary stage for all loops.

These results provide new constraints for future modeling efforts of the corona. Progress in the field over the past 30 years has meant that simply showing that our favorite heating mechanism or numerical experiment produces million degree temperatures is no longer sufficient. A viable model must reproduce the observed relationships between the magnetic properties of loops and the radiative signatures. As our results illustrate, the constraints from observations are significantly more precise than just a target temperature. Recent efforts looking at how models compare to constraints from emission measure distributions (Cargill 2014; Dahlburg et al. 2016; Barnes et al. 2016), time-lags (Bradshaw & Viall 2016), Doppler shifts (Hansteen et al. 2010; Zacharias et al. 2011; Bourdin et al. 2013) or non-thermal velocities (Olluri et al. 2015), are examples of the type of tests that numerical experiments need to pass before declaring success for any given theory. At this point, no experiment has been able to model active region heating, reproducing simultaneously a multiple set of constraints, such as emission measure distributions (i.e. emissivity at various temperatures), scaling with field strength, short-term variability, long-term decay, detailed morphology (i.e. topology), loop widths, etc. Significant progress has been made, however, in many of those areas independently.

Before we delve into the implications of our results for the heating rate, it is worth stopping to discuss other (non) dependencies. While it was not unexpected to find the scaling of intensity with B_{avg} , the fact that the Fe XVIII intensity is uncorrelated with field strength at the footpoints (B_f) does seem surprising. After all, the source of the energy in the system is expected to come from the convective motions at the surface where the feet of the loops are rooted, and there have been several studies arguing that the energy is preferentially deposited at the lower layers of the atmosphere: spicules contribution (De Pontieu et al. 2009, 2011), thermal non-equilibrium as a result of preferential footpoint heating (e.g. Mikić et al. 2013; Froment et al. 2017), predictions from 3D MHD resistive models (e.g. Gudiksen & Nordlund 2005; Hansteen et al. 2010; Reale et al. 2016). See also the broader remarks from Aschwanden et al. (2007) and the counter arguments from Klimchuk (2015) and references therein. Our results, where the intensity correlates with a quantity that depends on the field all along the loop, seem to be consistent with the coronal heating argument. We cannot, however, underestimate the limitations of current magnetic models. In fact, the spread of the solutions for each loop on the right panel of Figure 6 indicates that we still need to improve our understanding on how accurate the different magnetic models are in reproducing coronal conditions.

This study would not be complete if we did not discuss to some level the coronal heating implications of these loop measurements. As emission is only one by-product of heating in the atmosphere, to infer any of its underlying properties it is necessary to employ a model that describes how heating turns into emission at these wavelengths. Assuming that the evolving loops that we are observing can be modeled as independent single hydrodynamic structures, we use the “Enthalpy-based Thermal Evolution Loops” (EBTEL) model (Klimchuk et al. 2008; Cargill et al. 2012) to study the response of the plasma to heating. In particular, we are interested in how the Fe XVIII intensity scales with a heating that depends on B_{avg} and L . We have looked at a parameterization of the volumetric heating rate that scales as

$$\epsilon_H = \epsilon_0 \left(\frac{B_{avg}}{B_0} \right)^\alpha \left(\frac{L_0}{L} \right)^\beta \quad (1)$$

similar to our previous studies (Warren & Winebarger 2006, 2007; Ugarte-Urra et al. 2017). Following Warren & Winebarger (2006) we start by assuming $\epsilon_0 = 0.0492$ ergs cm $^{-3}$ s $^{-1}$ and $B_0 = 76$ G and $L_0 = 29$ Mm for an apex temperature close to 4 MK. For this work we find that $\epsilon_0 = 0.0738$ is a better choice to match the Fe XVIII intensities. That corresponds to a static equilibrium temperature of ~ 5 MK.

We computed the hydrodynamic response of all loops in our sample as determined by their B_{avg} and L as shown in bold font in Table 1. The heating time profile was assumed

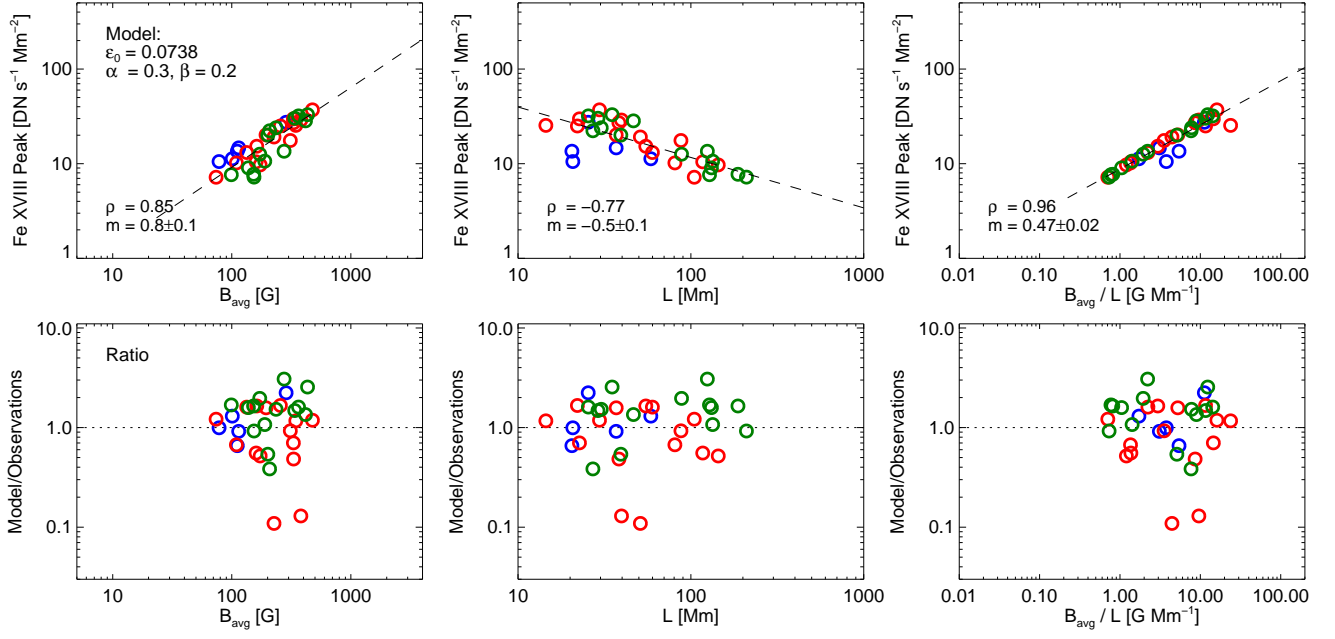


Figure 8. Dependence of the simulated Fe XVIII peak intensity as a function of B_{avg} and L . The top row shows the results of the model that best matches the observed slopes presented in Figures 6 and 7. The bottom row shows the ratio of model to observed intensities. The colors of the symbols have the same coding as previous figures.

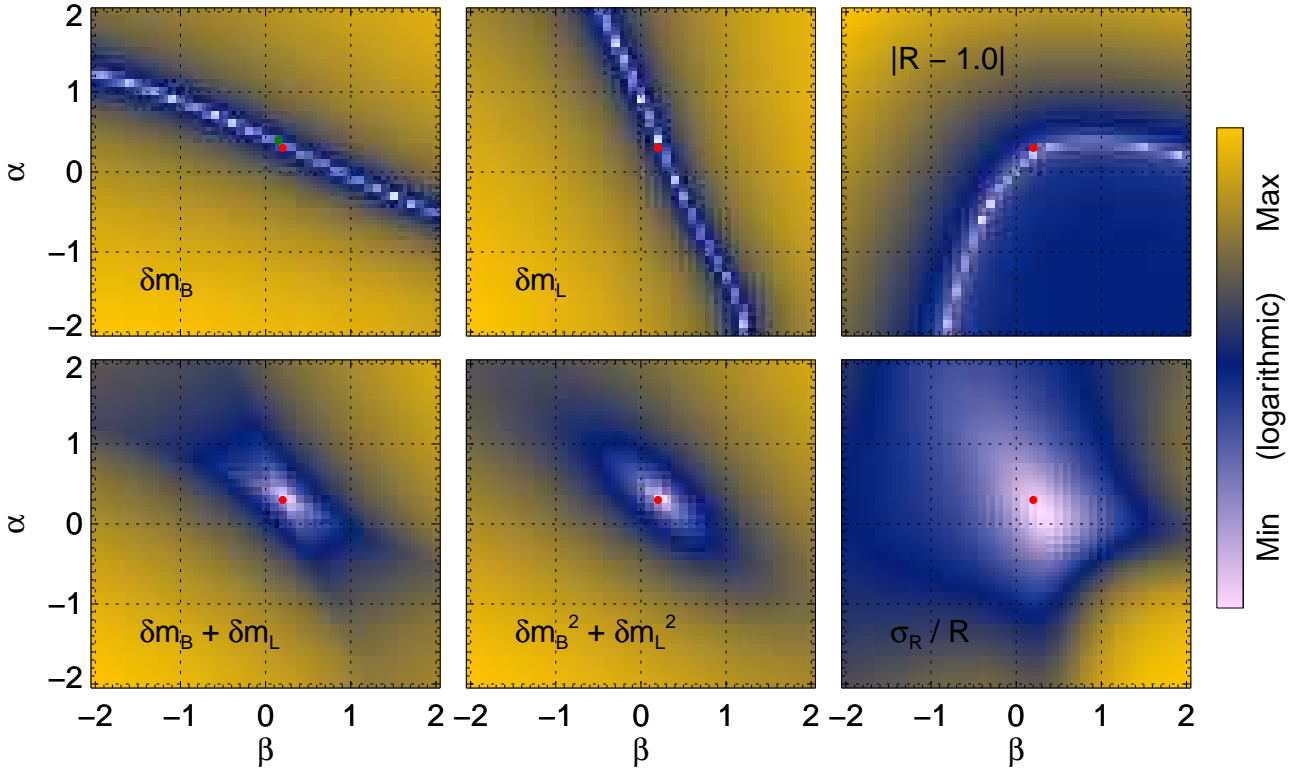


Figure 9. Parameter space explored when modeling impulsively heated loops with a volumetric heating rate parameterized as B_{avg}^α/L^β . The red symbol shows the best fit solution ($\alpha = 0.3$, $\beta = 0.3$) for the combined slopes ($\delta m_B + \delta m_L$ and $\delta m = |m_{model} - m_{obs}|$) of the Fe XVIII intensity dependence on B_{avg} and L . Also shown, the average ratio of intensities ($R = I_{model}/I_{obs}$) and standard deviation (σ_R).

as a 200s triangular pulse with a ϵ_H peak, over a steady background (static equilibrium temperature of 0.5 MK). From the temporal evolution of density and temperature, assuming 350 km radius loops (Ugarte-Urra et al. 2017), and the help of the CHIANTI atomic database (Dere et al. 1997; Del Zanna et al. 2015), we computed the AIA Fe XVIII lightcurves and recorded the peak time and intensity. For each loop we explored exponents α and β ranging [-2,2] in increments of 0.1. For each pair of exponents we calculated the dependence of the AIA Fe XVIII intensity with B_{avg} , L and the B_{avg}/L ratio and performed a linear fit to the power-law. The heating parameterization that best reproduces the observed slopes of the B_{avg} and L dependence is $\alpha = 0.3$ and $\beta = 0.2$. Within the uncertainties of the observed slopes, other pairs of solutions are still compatible, and lie in a diagonal where increasing α decreases β and viceversa. The approximate range is $\alpha = 0.3 \pm 0.2$ and $\beta = 0.2 \pm_{0.1}^{0.2}$, with $[\alpha, \beta] = [0.5, 0.1]$ and $[0.1, 0.4]$ at the extremes of the diagonal. Figure 8 shows the dependencies and the ratio of modeled to observed intensities for that case. Figure 9 shows the full parameter space of residuals resulting from comparing the slopes of the EBTEL modeling and AIA observations ($\delta m = |m_{model} - m_{obs}|$), with the minimum at $\alpha = 0.3$ and $\beta = 0.2$ for $\delta m_B + \delta m_L$ and $\delta m_B^2 + \delta m_L^2$. In the figure we also show the average ratio of intensities ($R = I_{model}/I_{obs}$) and the standard deviation (σ_R). Both also reach a valley around that solution.

This result compares well with several previous studies. Warren & Winebarger (2006) and Lundquist et al. (2008) found that a volumetric heating rate of $\epsilon_H \sim B_{avg}/L$, i.e. exponents $\alpha = 1$ and $\beta = 1$, provided the best agreement between full active region simulations made of ensembles of individually modeled loops and X-ray observations. Note that those studies only considered integers for the exponents. Even more interestingly, Winebarger et al. (2008), who added constraints from the EUV moss, provided a more precise estimate of $\epsilon_H \sim B_{avg}^{0.29 \pm 0.03}/L^{0.95 \pm 0.01}$ that is in full agreement with our estimate of α . We do not have an explanation for the discrepancy with β , but given the distribution of data points in Figure 6, with the two outliers at large intensities, it seems desirable to extend the relationship up to brighter loops to check if the slope becomes steeper or has multiple components.

There are other studies that are more difficult to compare with because their prescription of the heating depends on the footpoint field strength (B_f). Schrijver et al. (2004), in their full Sun models of the corona extending work in Schrijver & Aschwanden (2002), find that a heating flux density F_H (ergs cm⁻² s⁻¹) that scales as B_f/L provides the best match to X-ray and EUV observations. As $\epsilon_H \sim F_H/L$, then $\epsilon_H \sim B_f/L^2$. We have looked at the relationship between B_{avg} and B_f for our dataset and find

$B_f \sim B_{avg} L^{0.56 \pm 0.08}$. Replacing, that would mean $\epsilon_H \sim B_{avg}/L^{1.4}$, which is not consistent with our estimates given the uncertainties. Dudík et al. (2011) looking at full active regions and allowing for a spatially variable heating scale-length provide an estimate of $\epsilon_H \sim B_f^{0.7-0.8}/L^{0.5}$, i.e. $\epsilon_H \sim B_{avg}^{0.7-0.8}/L^{0.1}$ potentially consistent with our results if their uncertainties are of the same order. While the overall picture does not give us a complete agreement between all the various estimates, the trend of these results suggests that the volumetric heating rate scales with B_{avg}^α/L^β with exponents in the range 0.2–1.0.

5. CONCLUSION

We have investigated the magnetic (B_{avg} and L) and radiative (Fe XVIII 93.9Å intensities) properties of 34 loops from three active regions (NOAA 11158, 11190, 11339), with total unsigned fluxes spanning 4.2 – 26×10^{21} Mx, observed with the AIA and HMI instruments on board the *SDO* mission. These loops are formed at temperatures close to the peak of the emission measure in these active regions. We find that the peak intensity per unit cross-section of observed heating events in the loops scales proportionally with average magnetic field strength ($\sim B_{avg}^{0.9 \pm 0.3}$) and inversely with the loop length ($\sim L^{-0.6 \pm 0.2}$). We do not find any differences between loops from different regions. Furthermore, the intensities are uncorrelated with the field strength at the footpoints.

Our investigation shows that the relationship between intensity, field strength and loop length is compatible with impulsive heating with a volumetric heating rate $\epsilon_H \sim B_{avg}^{0.3 \pm 0.2}/L^{0.2 \pm_{0.1}^{0.2}}$. This result, obtained at the scale of individual loops, is compatible with several previous estimates obtained from full active region modeling as an ensemble of loops. While pinning down the scaling for ϵ_H may be a testable property of heating mechanisms as discussed by Mandrini et al. (2000) (see also Lundquist et al. 2008), the difficulty in finding ideal systems in the corona makes us think that the actual observables will become more powerful discriminators.

These results set new observational constraints for the major efforts currently underway in developing and testing the ability of state-of-the-art numerical experiments to reproduce observables in the corona. In combination with other constraints such as the relationship between morphology and magnetic topology, emission measure distributions, short and long-term variability, loop cross-sectional properties, Doppler-shifts, etc. they are setting a challenging, but definite description of the plasma properties in the corona that numerical renderings of the theories need to keep up with.

We would like to thank the anonymous referee for all the suggestions that helped improve the paper. I.U.U. acknowledges support by NASA under Grant No. NNH17AE96I issued through the Heliophysics Grand Challenge Research Program. H.P.W., N.A.C. were supported by the Chief of Naval Research and NASAs Hinode program. T.W. acknowledges DFG-grant WI 3211/5-1. The authors would like to

thank Markus Aschwanden for the comments and discussions on this work. AIA and HMI data are courtesy of NASA/SDO and the AIA and HMI science teams.

Facilities: SDO (AIA,HMI)

Software: CHIANTI (Dere et al. 1997; Del Zanna et al. 2015), SolarSoft (Freeland & Handy 2012)

REFERENCES

- Arregui, I. 2015, *Philosophical Transactions of the Royal Society of London Series A*, 373, 20140261
- Aschwanden, M., De Pontieu, B., & Katrukha, E. 2013, *Entropy*, 15, 3007
- Aschwanden, M. J. 2010, *SoPh*, 262, 399
- . 2016, *ApJS*, 224, 25
- Aschwanden, M. J., Winebarger, A., Tsiklauri, D., & Peter, H. 2007, *ApJ*, 659, 1673
- Barnes, W. T., Cargill, P. J., & Bradshaw, S. J. 2016, *ApJ*, 833, 217
- Benevolenskaya, E. E., Kosovichev, A. G., Lemen, J. R., Scherrer, P. H., & Slater, G. L. 2002, *ApJL*, 571, L181
- Berger, T. E., & Title, A. M. 1996, *ApJ*, 463, 365
- Borrero, J. M., & Ichimoto, K. 2011, *Living Reviews in Solar Physics*, 8, 4
- Bourdin, P. A., Bingert, S., & Peter, H. 2013, *A&A*, 555, A123
- Bradshaw, S. J., & Viall, N. M. 2016, *ApJ*, 821, 63
- Brooks, D. H., Warren, H. P., & Ugarte-Urra, I. 2012, *ApJ*, 755, L33
- Brooks, D. H., Warren, H. P., Ugarte-Urra, I., & Winebarger, A. R. 2013, *ApJ*, 772, L19
- Cargill, P. J. 2014, *ApJ*, 784, 49
- Cargill, P. J., Bradshaw, S. J., & Klimchuk, J. A. 2012, *ApJ*, 752, 161
- Dahlburg, R. B., Einaudi, G., Taylor, B. D., et al. 2016, *ApJ*, 817, 47
- Dahlburg, R. B., Einaudi, G., Ugarte-Urra, I., Rappazzo, A. F., & Velli, M. 2018, *ApJ*, 868, 116
- De Pontieu, B., McIntosh, S. W., Hansteen, V. H., & Schrijver, C. J. 2009, *ApJ*, 701, L1
- De Pontieu, B., McIntosh, S. W., Carlsson, M., et al. 2011, *Science*, 331, 55
- Del Zanna, G., Dere, K. P., Young, P. R., Landi, E., & Mason, H. E. 2015, *A&A*, 582, A56
- Démoulin, P. 2004, in *IAU Symposium*, Vol. 223, *Multi-Wavelength Investigations of Solar Activity*, ed. A. V. Stepanov, E. E. Benevolenskaya, & A. G. Kosovichev, 13–22
- Dere, K. P., Landi, E., Mason, H. E., Monsignori Fossi, B. C., & Young, P. R. 1997, *A&AS*, 125, 149
- Dudík, J., Dzifčáková, E., Karlický, M., & Kulinová, A. 2011, *A&A*, 531, A115
- Fisher, G. H., Longcope, D. W., Metcalf, T. R., & Pevtsov, A. A. 1998, *ApJ*, 508, 885
- Fludra, A., & Ireland, J. 2008, *A&A*, 483, 609
- Fludra, A., Ireland, J., Del Zanna, G., & Thompson, W. T. 2002, *Advances in Space Research*, 29, 361
- Freeland, S. L., & Handy, B. N. 2012, *SolarSoft: Programming and data analysis environment for solar physics*, *Astrophysics Source Code Library*, record ascl:1208.013, , , ascl:1208.013
- Froment, C., Auchère, F., Aulanier, G., et al. 2017, *ApJ*, 835, 272
- Gudiksen, B. V., & Nordlund, Å. 2005, *ApJ*, 618, 1020
- Hansteen, V. H., Hara, H., De Pontieu, B., & Carlsson, M. 2010, *ApJ*, 718, 1070
- Klimchuk, J. A. 2006, *SoPh*, 234, 41
- . 2015, *Philosophical Transactions of the Royal Society of London Series A*, 373, 20140256
- Klimchuk, J. A., Patsourakos, S., & Cargill, P. J. 2008, *ApJ*, 682, 1351
- Lemen, J. R., Title, A. M., Akin, D. J., et al. 2012, *SoPh*, 275, 17
- López Fuentes, M. C., Klimchuk, J. A., & Mandrini, C. H. 2007, *ApJ*, 657, 1127
- Lundquist, L. L., Fisher, G. H., Metcalf, T. R., Leka, K. D., & McTiernan, J. M. 2008, *ApJ*, 689, 1388
- Mandrini, C. H., Démoulin, P., & Klimchuk, J. A. 2000, *ApJ*, 530, 999
- Mikić, Z., Lionello, R., Mok, Y., Linker, J. A., & Winebarger, A. R. 2013, *ApJ*, 773, 94
- O’Dwyer, B., Del Zanna, G., Mason, H. E., Weber, M. A., & Tripathi, D. 2010, *A&A*, 521, A21
- Olluri, K., Gudiksen, B. V., Hansteen, V. H., & De Pontieu, B. 2015, *ApJ*, 802, 5
- Pesnell, W. D., Thompson, B. J., & Chamberlin, P. C. 2012, *SoPh*, 275, 3
- Pevtsov, A. A., Fisher, G. H., Acton, L. W., et al. 2003, *ApJ*, 598, 1387
- Porter, L. J., & Klimchuk, J. A. 1995, *ApJ*, 454, 499
- Reale, F. 2014, *Living Reviews in Solar Physics*, 11, 4
- Reale, F., Orlando, S., Guarrasi, M., et al. 2016, *ApJ*, 830, 21

- Scherrer, P. H., Schou, J., Bush, R. I., et al. 2012, *SoPh*, 275, 207
- Schrijver, C. J. 1987, *A&A*, 180, 241
- Schrijver, C. J., & Aschwanden, M. J. 2002, *ApJ*, 566, 1147
- Schrijver, C. J., Sandman, A. W., Aschwanden, M. J., & De Rosa, M. L. 2004, *ApJ*, 615, 512
- Scott, J. T., Martens, P. C. H., & McKenzie, D. E. 2012, *SoPh*, 276, 113
- Testa, P., De Pontieu, B., Allred, J., et al. 2014, *Science*, 346, 1255724
- Tiwari, S. K., Thalmann, J. K., Panesar, N. K., Moore, R. L., & Winebarger, A. R. 2017, *ApJ*, 843, L20
- Ugarte-Urra, I., Upton, L., Warren, H. P., & Hathaway, D. H. 2015, *ApJ*, 815, 90
- Ugarte-Urra, I., & Warren, H. P. 2014, *ApJ*, 783, 12
- Ugarte-Urra, I., Warren, H. P., & Brooks, D. H. 2009, *ApJ*, 695, 642
- Ugarte-Urra, I., Warren, H. P., Upton, L. A., & Young, P. R. 2017, *ApJ*, 846, 165
- Ugarte-Urra, I., Warren, H. P., & Winebarger, A. R. 2007, *ApJ*, 662, 1293
- Ugarte-Urra, I., Winebarger, A. R., & Warren, H. P. 2006, *ApJ*, 643, 1245
- van Driel-Gesztelyi, L., Démoulin, P., Mandrini, C. H., Harra, L., & Klimchuk, J. A. 2003, *ApJ*, 586, 579
- van Driel-Gesztelyi, L., & Green, L. M. 2015, *Living Reviews in Solar Physics*, 12, 1
- Viall, N. M., & Klimchuk, J. A. 2012, *ApJ*, 753, 35
- Warren, H. P., Crump, N. A., Ugarte-Urra, I., et al. 2018, *ApJ*, 860, 46
- Warren, H. P., Ugarte-Urra, I., Doschek, G. A., Brooks, D. H., & Williams, D. R. 2008, *ApJL*, 686, L131
- Warren, H. P., & Winebarger, A. R. 2006, *ApJ*, 645, 711
- , 2007, *ApJ*, 666, 1245
- Warren, H. P., Winebarger, A. R., & Brooks, D. H. 2012, *ApJ*, 759, 141
- Wiegelmann, T., & Sakurai, T. 2012, *Living Reviews in Solar Physics*, 9, 5
- Wiegelmann, T., Thalmann, J. K., Inhester, B., et al. 2012, *SoPh*, 281, 37
- Winebarger, A. R., & Warren, H. P. 2004, *ApJL*, 610, L129
- , 2005, *ApJ*, 626, 543
- Winebarger, A. R., Warren, H. P., & Falconer, D. A. 2008, *ApJ*, 676, 672
- Xie, H., Madjarska, M. S., Li, B., et al. 2017, *ApJ*, 842, 38
- Zacharias, P., Peter, H., & Bingert, S. 2011, *A&A*, 531, A97